

## Research report

## MRI detection of ferritin iron overload and associated neuronal pathology in iron regulatory protein-2 knockout mice

Colette Grabill<sup>a,b</sup>, Afonso C. Silva<sup>c</sup>, Sophia S. Smith<sup>a</sup>, Alan P. Koretsky<sup>c</sup>,  
Tracey A. Rouault<sup>a,\*</sup><sup>a</sup>Cell Biology and Metabolism Branch, National Institute of Child Health and Human Development, Bldg. 18T, Room 101 9000 Rockville Pike, Bethesda, MD 20892, USA<sup>b</sup>Uniformed Services University of the Health Sciences, Bethesda, MD, USA<sup>c</sup>Laboratory of Functional and Molecular Imaging, National Institute of Neurological Disorders and Stroke, Bethesda, MD, USA

Accepted 24 January 2003

---

**Abstract**

Genetic ablation of iron regulatory protein 2 (IRP-2), a protein responsible for post-transcriptional regulation of expression of several iron metabolism proteins, predisposes IRP-2  $-/-$  mice to develop adult onset neurodegenerative disease. Ferric iron reproducibly accumulates within axonal tracts and neuronal cell bodies in discrete regions of the brain, and areas of iron accumulation colocalize with areas of high ferritin expression. To better evaluate the onset and progression of neurodegeneration in IRP-2  $-/-$  mice, we performed a high-resolution magnetic resonance imaging study comparing live, age-matched wild-type and IRP-2  $-/-$  mice, using an 11.7-Tesla magnet and a custom-designed head coil. The mice were perfused after imaging, and iron stains and immunohistochemical studies were performed. We detected increases in the number of pixels with low  $T_2$  values expected from accumulations of iron in IRP-2  $-/-$  mice. Moreover, in several areas of the brain, including the substantia nigra and the superior colliculus, we detected areas with unusually high  $T_2$  values that likely represented accumulation of water. On histopathological examination we discovered relatively small vacuoles in these brain regions of IRP-2  $-/-$  mice. Our ability to gather  $T_2$  data within regions of interest enabled us to define a bimodal  $T_2$  intensity pattern that likely represents both ferritin iron accumulation and its associated pathological consequences within the brain. Our discoveries may have significant applications for the diagnosis and treatment of human diseases if such high-resolution techniques can be adapted for use in human subjects.

© 2003 Elsevier Science B.V. All rights reserved.

*Theme:* Disorders of the nervous system*Topic:* Genetic models*Keywords:* Iron regulatory protein; Ferritin; Vacuolization; Neurodegenerative disease; Brain; Magnetic resonance imaging

---

Recently, inherited abnormalities of iron metabolism proteins have been shown to cause disease in humans [8] and mice [2,15,19,26]. Mice with a targeted deletion of iron regulatory protein 2 (IRP-2) overexpress ferritin and develop progressive neurodegenerative disease [19]. IRP-2 is one of two mammalian cytosolic proteins that senses iron and represses ferritin synthesis in iron-depleted cells [1,28]. Mice that lack IRP-2 develop progressive tremors, proximal muscle weakness, and ataxia. Serum ferritin is

elevated compared to wild-types, and ferritin immunohistochemistry shows overexpression of ferritin in certain brain regions. Increased iron staining colocalizes with areas of ferritin overexpression and neurodegeneration, leading us to believe that misregulation of ferritin synthesis and maldistribution of iron causes the observed neurodegeneration in IRP-2  $-/-$  mice.

Magnetic resonance imaging is a non-invasive method increasingly utilized to evaluate human patients with neurodegenerative disorders. Accurate description of a distinctive MRI pattern for different diseases could lead to earlier diagnosis, assist in following disease progression, and help to elucidate whether the iron accumulation is a

---

\*Corresponding author. Tel.: +1-301-496-7060; fax: +1-301-402-0078.

E-mail address: [trou@helix.nih.gov](mailto:trou@helix.nih.gov) (T.A. Rouault).

cause or a consequence of the pathology. The underlying principle of visualizing iron on MRI is that the iron storage protein ferritin has a superparamagnetic core which disrupts the magnetic field and produces a lower (darker) signal on  $T_2$  weighted images [11]. Many MRI studies of human patients with neurodegenerative diseases have been reported [3,18,24], and perfused brains from rats with a mutation in DMT1 have been imaged [38], but to the best of our knowledge, MRI has not been previously used to study iron overload in mice with neurodegenerative disease.

The objective of our study was to utilize MRI as a tool for non-invasive detection of brain iron accumulation and associated pathology in IRP-2  $-/-$  mice. We initially hypothesized that overexpression of ferritin and increased iron deposition in specific brain regions of IRP-2  $-/-$  mice would result in detection of lower  $T_2$  values (darker areas) in affected areas of the brain. In this study, we confirmed that we could reliably detect lower  $T_2$  values in areas of the brain known to accumulate ferritin iron in IRP-2  $-/-$  mice. In addition, we generated histograms that represent the full spectrum of high-resolution  $T_2$  values from several regions of interest and discovered a second unexpected abnormality. Several areas of the brain contained higher intensities (longer  $T_2$ ) that are most consistent with increased water content within brain parenchyma, and/or decreases in iron content. Histological examination of the brains showed the presence of previously unappreciated fluid filled vacuoles, which may help to explain both the MRI data and the neurological disorder seen in IRP-2  $-/-$  mice.

## 1. Methods

### 1.1. Control versus knockout groups

Twenty-two mice ranging in age from 6 to 14 months were used in this study. The animals were divided into a control group, consisting of 11 C57/BL6 mice (six males, five females, mean age 9.5 months, mean weight 33.6 g), and the knockout group consisting of 11 IRP-2  $-/-$  mice (six males, five females, mean age 9.5 months, mean weight 31.5 g). Genotyping of each animal was done by Southern Blot analysis [19]. On the days of the MRI experiments, one or two mice from the knockout group were individually paired for sex, age, and weight with mice from the control group. Although formal motor and balance testing was not performed prior to imaging, all of the IRP-2  $-/-$  animals in this study had easily visible phenotypical changes including ataxia, tremor, hind leg weakness, and poor grooming habits.

### 1.2. Animal preparation

Mice were anesthetized by inhalation of 1.5–2% iso-

flurane in a gas mixture of 50%  $N_2$ :50%  $O_2$  delivered through a face mask during the entire procedure. To prevent motion during the scans, the mice were fitted to a custom-built head holder consisting of a bite bar placed inside the facemask. Body temperature was monitored using a rectal probe and maintained greater than 35 °C using a warm water pad placed underneath their body. After imaging, animals recovered by breathing room air while still on the warm water pad.

### 1.3. MRI methods

All images were acquired using an 11.7-T/31-cm horizontal magnet (Magnex, Abingdon, UK), interfaced to a Bruker AVANCE console (Bruker, Billerica, MA). Images were acquired using an 89-mm Helmholtz transmit RF coil and an 8×15-mm ellipsoidal receive surface RF coil, built to conform to the shape of the mouse skull so as to optimize signal-to-noise over the entire mouse brain. After positioning the mouse head in the magnet isocenter, global shimming was performed, and tri-pilot spin-echo scout images were obtained to aid slice positioning for the multi-slice  $T_2$  maps. Twenty-four, 250- $\mu$ m thick coronal slices were chosen spaced 500  $\mu$ m apart to cover most of the brain, from the cerebellum to the olfactory bulb.  $T_2$  maps were obtained using a Carr, Purcell, Meiboom, Gill (CPMG) multi-echo spin-echo sequence with the following parameters: field of view (FOV)=2.56×2.56 cm<sup>2</sup>; matrix size=256×256; slice thickness=250  $\mu$ m; NEX=1; repetition time (TR)=10 s; inter-echo time (TE)=10 ms; number of echoes=8. The corresponding nominal resolution of each pixel was 100×100×250  $\mu$ m<sup>3</sup>.  $T_1$  weighting of the images was avoided by the long TR, and the range of echo times (10–80 ms) was adequate for sampling  $T_2$  values shorter and longer than the average  $T_2$  for brain tissue at 11.7 T, which in our study is approximately 35 ms (see Section 2). Total scan acquisition time was on the order of 42 min. The typical signal-to-noise ratio (SNR) for this sequence was 56:1.

### 1.4. Data and image analysis

$T_2$  maps were obtained on a pixel-by-pixel basis by fitting each pixel to a two-parameter mono-exponential curve, using Bruker's ParaVision Curve Fitting Algorithm. Seven distinct anatomical regions of the brain were chosen for region-of-interest (ROI) analysis of  $T_2$  values. Cerebellar white matter, superior colliculus, substantia nigra, interpeduncular nucleus, fornix, and fimbria of hippocampus were either previously known to be affected by iron misregulation in IRP-2  $-/-$  mice, or predicted to accumulate iron based on low  $T_2$  values obtained from preliminary pilot studies. The seventh region, the cortex, an area of the brain that does not accumulate significant amounts of iron based on Perls' DAB staining in our IRP-2  $-/-$  mouse model [19], was used as a control.

ROIs were obtained by carefully outlining an entire anatomical region without including any surrounding structures.  $T_2$  histograms were obtained from the pixels within each ROI, and statistical analysis was performed on the histograms. The mean  $T_2$  value and the standard deviation of individual  $T_2$  histograms were computed. We noticed that the standard deviations of histograms in the IRP-2  $-/-$  group were consistently larger than in the wild-type group, suggesting that the knockout mice presented a broader range of  $T_2$  values. To better measure the dispersion of the histograms, we computed the ratio mean  $T_2$ /S.D. and compared the two groups. Student  $t$ -tests were run for each ROI to determine statistical differences. In addition, an average histogram was obtained for each ROI by summing the individual histograms from each mouse in each of the two groups. These averaged histograms were fit to a gamma variate function of the type:

$$I(T_2) = A \cdot (T_2 - B)^C \cdot e^{-\left(\frac{T_2 - B}{D}\right)} \quad (1)$$

Mean  $T_2$  and standard deviation were computed from the best fits to the region-specific averaged histograms and reported. Statistical difference between the fits to data from the IRP-2  $-/-$  group and the wild-type group was assessed by a paired  $t$ -test on all ROIs except the cortex.

Data are presented as mean  $\pm$  S.D. Unless otherwise specified, differences were considered statistically significant at  $P < 0.05$ .

### 1.5. Histology

One to 2 days after imaging, mice from both groups were perfusion fixed. They were anesthetized with 0.3 mg pentobarbital prior to the procedure, and perfused with phosphate-buffered saline wash (pH 7.4), followed by 4% paraformaldehyde fix. The brains remained within the skull overnight in 4% paraformaldehyde at 4 °C. The brains were then carefully removed and sent for histological sectioning (American Histo Labs, Gaithersburg, MD). The brains were cut in 7- $\mu$ m thick coronal sections and placed on sialinated slides. Hematoxylin and eosin stain was used to identify anatomy. We stained sequential sections with Perls' DAB for ferric iron and performed ferritin immunohistochemistry.

For Perls' DAB staining, the slides were dewaxed in xylene, rehydrated using sequentially decreasing concentrations of ethanol, washed in TBS Buffer, and treated with a 1:1 solution of 2% HCl and 2% KFeCN for 40 min. The tissues were again washed in the same buffer and treated for 35 min with DAB–Tris– $H_2O_2$ . They were dehydrated in increasing concentrations of ethanol, cleared in xylene, and mounted on slides using permount.

Ferritin immunohistochemistry was performed using prediluted ferritin antibody (Biogenesis, Kingston, NH) per the manufacturer's recommendations. We used goat anti-

rabbit IgG conjugated to biotin as the secondary antibody (Vector Laboratories, Burlingame, CA), followed by avidin–biotin complex labeled with horseradish peroxidase (ABC Elite Kit, Vector Laboratories, Burlingame, CA). HRP was visualized using the substrate diaminobenzidine (DAB, Vector Laboratories) with incubation at room temperature for 1 h and counterstained with methyl green.

Three 9-month-old IRP-2  $-/-$  and three age-matched wild-type animals were also perfusion fixed with 2% glutaraldehyde, epoxy embedded, and stained with toluidine blue and safranin by Dr. Bernard Jortner of Virginia Polytechnic Institute, Blacksburg, VA, to allow reliable evaluation of brain morphology (method discussed in Ref. [13]).

## 2. Results

Fig. 1 shows typical MR coronal images of the mouse brain obtained at 11.7 T. The left column shows  $T_2$ -weighted images from a wild-type mouse (top) and from an IRP-2  $-/-$  mouse (bottom). The  $T_2$ -weighted images show excellent contrast between gray and white matter. In the IRP-2  $-/-$  mouse (bottom left), significant heterogeneities in signal intensities can be noticed in white matter tracts, such as the cingulum, and in medial regions, such as the superior colliculus and the interpeduncular nucleus. In order to better identify regions of altered  $T_2$  contrast between wild-type and IRP-2  $-/-$  mice, quantitative  $T_2$  maps were obtained. The right column of Fig. 1 shows the corresponding  $T_2$  maps from the same slices shown in the left column. The grayscale bar shows the range of  $T_2$  values in the  $T_2$  maps. Regional heterogeneities in  $T_2$  values can be easily identified both in the wild-type as well as in the IRP-2  $-/-$  mouse brain. In addition, some regions, such as the interpeduncular nucleus, tended to have lower  $T_2$  values in the knockout mice compared to the wild-type mice (Fig. 1, right column).

Seven ROIs were chosen for comparison of  $T_2$  values between the control and knockout groups. Fig. 2 shows an example of designated ROIs. Mean  $T_2$  values were calculated for each ROI. These  $T_2$  averages were then compared between groups. We predicted that we would find lower  $T_2$  values from IRP-2  $-/-$  mice compared to wild-type mice. Surprisingly, the average  $T_2$  values of the specified regions were not significantly different between the IRP-2  $-/-$  and control groups, as shown in Table 1. Nevertheless, the dispersion of  $T_2$  values within all ROIs except the cortex was significantly broader for the knockout group (Table 1). This broader dispersion, measured both from the standard deviation of the average  $T_2$  values, as well as from an index expressed by the average  $T_2$  divided by the standard deviation, may be indicative of altered iron distribution in the brains of the IRP-2  $-/-$  mice.

To further study the distribution of  $T_2$  values, histograms were created for each ROI. A consistent difference

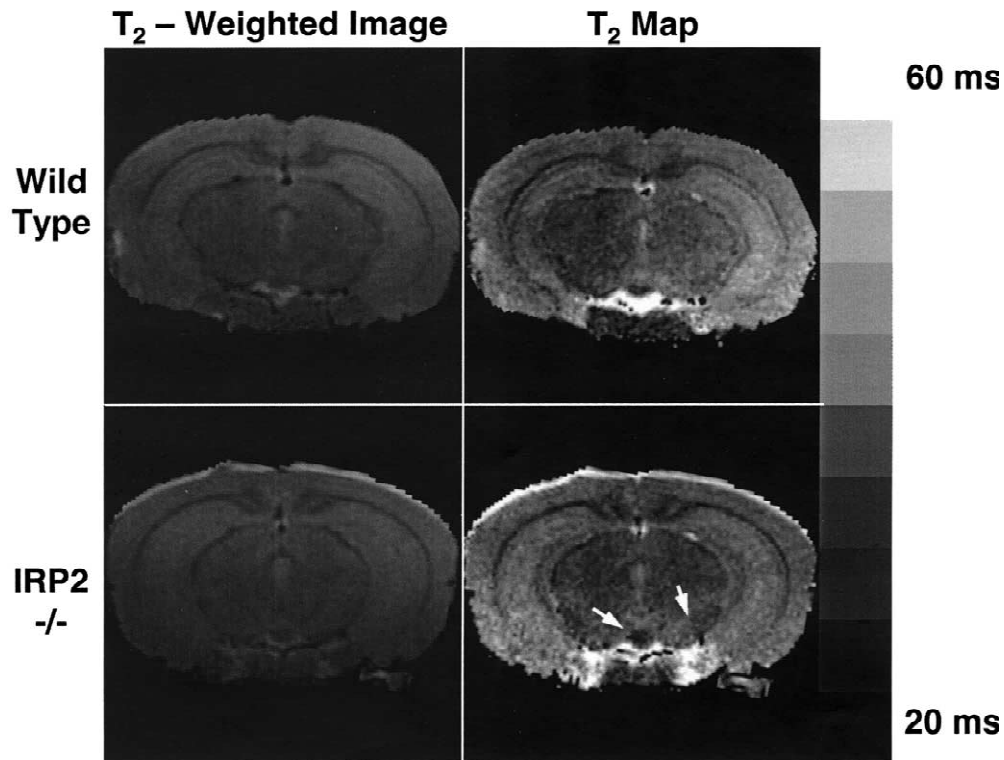


Fig. 1. Comparison of wild-type and IRP-2  $-/-$  anatomical  $T_2$ -weighted images and quantitative  $T_2$  maps. High-resolution ( $100 \times 100 \times 250 \mu\text{m}^3$ ) spin-echo  $T_2$ -weighted coronal images (left) and corresponding  $T_2$  maps (right) were used for identifying regions of altered iron accumulation in IRP-2  $-/-$  mice, compared to wild types. Note that several areas in the IRP-2  $-/-$  mouse (bottom), such as the interpeduncular nucleus and the substantia nigra (arrows), appear darker than the corresponding regions in the wild-type mouse (top) both in the  $T_2$ -weighted image as well as in the  $T_2$  map.

in the distribution of  $T_2$  values between the wild-type and IRP-2  $-/-$  groups was detected (filled symbols in Fig. 3). The distribution of the wild-type group was symmetric with a peak in the mid-range of  $T_2$  values for all ROIs, whereas in the IRP-2  $-/-$  group, a broader and asymmetric distribution of signal intensity was appreciable within the ROIs. For example, the histogram obtained from the

IRP-2  $-/-$  fornix data showed an expected increase in the frequency of occurrence of pixels with shorter  $T_2$  values, consistent with increased ferritin iron (note the asymmetry in Fig. 3a). In other IRP-2  $-/-$  regions of interest (Fig. 3b–f), particularly in the superior colliculus (Fig. 3e) and the substantia nigra (Fig. 3f), an increase in frequency of occurrence of short  $T_2$  pixels similar to the

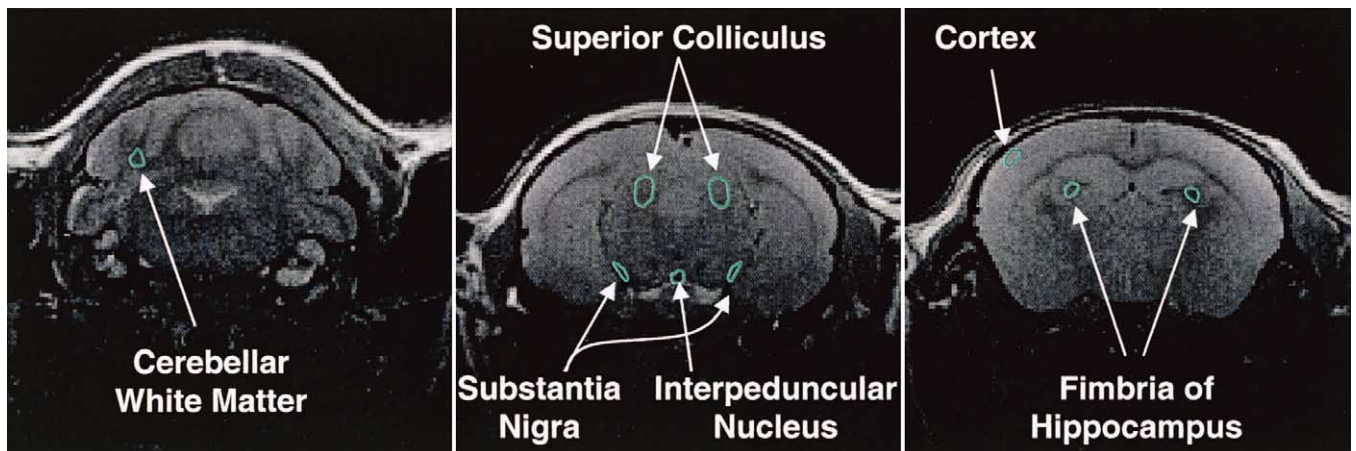


Fig. 2. Region of interest selection. ROIs were selected based on histological findings of increased iron in our prior studies of IRP-2  $-/-$  mice as well as on pilot MRI data that revealed regions with low  $T_2$  values in the IRP-2  $-/-$  mice. Circled areas identify the anatomical regions that were analyzed (fornix not shown).  $T_2$  values were extracted from all pixels in each ROI and compared between the IRP-2  $-/-$  and control groups.

Table 1  
Comparison of average  $T_2$  and dispersion between IRP-2  $-/-$  and wild type groups

Region	IRP2 $-/-$		Wild type	
	$T_2^a$ (ms)	$\frac{\text{Mean } T_2^c}{\text{S.D.}}$	$T_2^a$ (ms)	$\frac{\text{Mean } T_2^c}{\text{S.D.}}$
Cerebellar white matter	$34.13 \pm 3.204$	$11.09 \pm 2.29$	$32.22 \pm 2.43$	$13.88 \pm 2.98$
Superior colliculus	$34.14 \pm 2.98^b$	$11.93 \pm 2.56$	$32.45 \pm 2.60^b$	$13.36 \pm 3.66$
Interpeduncular nucleus	$36.24 \pm 4.28$	$9.03 \pm 2.80$	$35.87 \pm 3.36$	$11.58 \pm 4.31$
Substantia nigra	$36.63 \pm 4.10$	$9.47 \pm 2.20$	$35.01 \pm 3.22$	$11.46 \pm 2.95$
Fimbria	$32.24 \pm 3.10$	$10.67 \pm 1.88$	$32.03 \pm 2.73$	$12.50 \pm 3.16$
hippocampus				
Fornix	$32.41 \pm 3.29$	$10.89 \pm 3.30$	$34.00 \pm 2.31$	$15.71 \pm 5.08$
Cortex <sup>d</sup>	$35.84 \pm 4.35$	$13.56 \pm 11.54$	$34.95 \pm 3.02$	$14.27 \pm 6.58$

<sup>a</sup> Mean  $T_2$  values from all regions except the superior colliculus are not significantly different between groups ( $P > 0.07$ ). However, for all regions except cortex, the standard deviation values are significantly larger in the IRP-2  $-/-$  group ( $P < 0.04$ ).

<sup>b</sup> The mean  $T_2$  value from the superior colliculus is significantly longer in the IRP-2  $-/-$  group ( $P < 0.02$ ).

<sup>c</sup> The dispersion ratio Mean  $T_2$ /S.D. from all regions except the cortex is significantly smaller in the IRP-2  $-/-$  group ( $P < 0.05$ ).

<sup>d</sup> Neither the mean  $T_2$  value, nor its standard deviation, nor the dispersion ratio Mean  $T_2$ /S.D. from the cortex were significantly different ( $P > 0.22$ ) between the groups.

fornix pattern was found along with an unexpected and notable increase in the number of pixels with longer  $T_2$  values. Not only were these patterns distinctly asymmetric, but they manifested a bi-modal peak compared to the wild-type single peak distribution. The pattern of distribution for the control region (cortex) was similar between the two groups, as seen in Fig. 3g, and was not suggestive of iron accumulation in the IRP-2  $-/-$  mice.

To verify the significance of the different patterns of  $T_2$  value distribution between the IRP-2  $-/-$  and wild-type groups, the histogram data was analyzed using a gamma variate fit method (solid lines in Fig. 3). This statistical test is frequently used in magnetic resonance imaging to detect variation in the distribution of data points [4,9,27]. The gamma variate fit was used to determine the average  $T_2$  and to calculate the dispersion of the histogram. These data are shown in Table 2. No significant difference was detected in the average  $T_2$  between the groups, consistent with the ROI analysis. In all areas except the cortex, there was a significant difference in the dispersion of the fit, with the IRP-2  $-/-$  mice presenting a significantly wider distribution of  $T_2$  values.

In the anatomical regions of the IRP-2  $-/-$  mice where MRI abnormalities were noted, Perls' DAB stained coronal slices of the imaged and perfused brain showed dark brown regions indicative of ferric iron deposition (Fig. 4). Ferritin immunohistochemistry showed increased ferritin accumulation in the same regions of the IRP-2  $-/-$  mouse (Fig. 5), supporting the previous observation that ferritin is over-expressed in IRP-2  $-/-$  mice [19]. The Perls' DAB stains and ferritin immunohistochemistry did not show iron accumulation or ferritin over-expression in the wild-type mouse (Figs. 4 and 5).

To obtain better preservation of brain tissue for assessment of neuropathology, brain tissue from three 9-month-old IRP-2  $-/-$  mice and three 9-month-old wild-type

mice was epoxy embedded following perfusion and was stained with toluidine blue and safranin counterstain. Using light microscopy, vacuoles ranging in size from 15 to 25  $\mu\text{m}$  were identified within the substantia nigra pars compacta and the superior colliculus of the IRP-2  $-/-$  mice (Fig. 6). Using the same histological method, neurons in various stages of degeneration were identified. Detachment of the neuronal cell body from the surrounding tissue was observed, along with disorganization of the cytosol, shrinkage of the nucleus, and dissolution of the nuclear membrane (not shown). These degenerative changes seen in neurons in the substantia nigra and superior colliculus of the 9-month-old IRP-2  $-/-$  mice, but not in their wild-type counterparts, likely precede formation of detectable vacuoles (Fig. 6).

### 3. Discussion

Iron is required in the central nervous system to facilitate important cellular functions including electron transport, myelination of axons, and synthesis of neurotransmitters. Iron deficiency, as well as iron overload, can be deleterious to the central nervous system, and balancing the beneficial and harmful effects is an essential aspect of cell survival. Detailed studies of brain iron distribution in normal humans [17,22], as well as in mice [16], have been published, and it is well established that abnormal brain iron deposition causes oxidative damage to lipids, carbohydrates, proteins and nucleic acids (reviewed in Ref. [6]). Iron accumulation has been implicated in the progression of many human neurodegenerative diseases including Parkinson's disease, multiple system atrophy, Alzheimer's disease and neuronal brain iron accumulation type 1 (formerly known as Hallervorden–Spatz syndrome) [5,10,12,20,32,37]. Although the role of iron deposition in



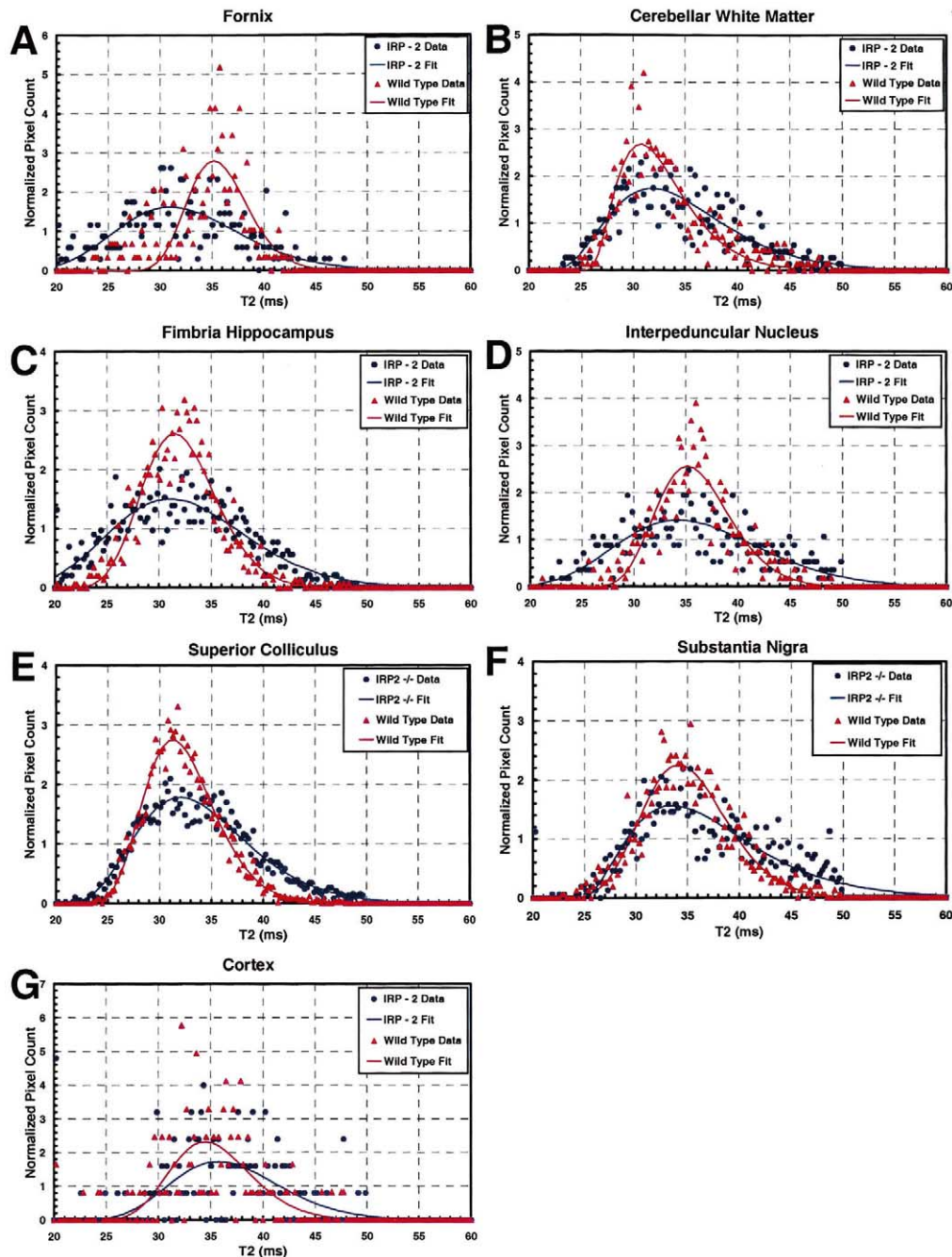


Fig. 3.  $T_2$  histograms and gamma variate fit of regions of interest. Histograms were computed from the  $T_2$  values of the multiple individual pixels comprising each region of interest. The relative pixel frequency of occurrence is represented on the Y-axis and the  $T_2$  value in milliseconds is represented on the X-axis. Gamma variate fits to the  $T_2$  histograms are represented by the solid lines. The histogram pattern for the cortex (g) is not different between the IRP-2  $-/-$  and wild-type groups, but all other histograms show a broader  $T_2$  distribution in the IRP-2  $-/-$  group. In all regions other than the cortex (g), the dispersion of the fits to the IRP-2  $-/-$  group is significantly broader than the wild-type group.

these neurodegenerative processes remains uncertain, iron accumulations are often found in affected regions. The question remains whether the changes in local iron accumulation are primary or secondary events in the pathophysiology of these diseases.

Using high-resolution MRI, we evaluated 11 matched pairs of wild-type and IRP-2  $-/-$  mice and discovered

that there was a difference in distribution of  $T_2$  values between groups. The histograms showed a significant difference between IRP-2  $-/-$  and wild-type mice, with the IRP-2  $-/-$  mice showing a broader distribution of values. In many of the regions studied there were pixels showing shorter  $T_2$  values consistent with increased iron in the IRP-2  $-/-$  mice. We demonstrated with Perl's DAB

Table 2  
Analysis of gamma variate fit to  $T_2$  histograms

Region	IRP2 $-/-$		Wild type	
	$T_2$ (ms) <sup>a</sup>	$\frac{\text{Mean } T_2}{\text{S.D.}}$ <sup>b</sup>	$T_2$ (ms) <sup>a</sup>	$\frac{\text{Mean } T_2}{\text{S.D.}}$ <sup>b</sup>
Cerebellar white matter	31.83±5.37	5.93	30.76±3.2	9.61
Superior colliculus	32.03±5.27	6.08	31.28±3.36	9.31
Interpeduncular nucleus	34.33±6.79	5.06	35.18±3.51	10.02
Substantia nigra	33.56±5.83	5.76	34.15±4.07	8.39
Fimbria	31.04±6.44	4.82	31.5±3.53	8.92
hippocampus				
Fornix	31.01±5.87	5.28	35.17±2.88	12.21
Cortex	35.73±5.14	6.95	34.47±3.82	9.02

<sup>a</sup> Mean  $T_2$  values are not significantly different between groups ( $P > 0.19$ ). However, the standard deviation values are significantly larger in the IRP-2  $-/-$  group ( $P < 0.0001$ ).

<sup>b</sup> The dispersion ratio Mean  $T_2$ /S.D. is significantly smaller in the IRP-2  $-/-$  group ( $P < 0.002$ ).

stains and immunohistochemistry that the regions of interest were rich in ferric iron and ferritin, consistent with previous findings from these mice.

In addition to the expected increase of pixels with shorter  $T_2$  values, many of the ROIs in the IRP-2  $-/-$  mice also showed an increase in the number of pixels with longer  $T_2$  values. Increases in  $T_2$  could be caused by decreases in ferritin iron within discrete pixels or by increases in fluid accumulation within pixels. Iron stains from ROIs did not reveal focal areas of iron depletion within intact tissue. However, fluid-filled vacuoles were detected within the parenchyma of epoxy embedded IRP-2  $-/-$  brains using light microscopy. In the toluidine blue and safranin stained epoxy embedded sections, we identified neurons within the substantia nigra and superior colliculus that appeared to be at various different stages of degeneration. We also discovered many ‘empty holes’ in which remnants of nuclei and traces of debris were found. The process appeared to begin with the neuronal cell membrane separating from the surrounding tissue, developing a ‘necklace-like’ ring of detachment. This untethering was followed by loss of nuclear and cell membrane integrity, and general disorganization of the cell. We propose that these neurons degenerate, undergo phagocytosis, and are ultimately replaced by fluid-filled vacuoles. The size of many of the vacuoles is comparable to the size of neuronal cell bodies in these regions. These vacuoles were easily distinguished from blood vessels since the vacuoles lack endothelial-lining cells and were not found in similarly perfused wild-type mice. Three wild-type animals were compared to three IRP-2  $-/-$  mice, and a marked statistical increase in vacuolization was noted in the IRP-2  $-/-$  (Smith, S., and Rouault, T.A., manuscript in preparation).

Vacuoles found in the central nervous system of humans are usually associated with spongiform encephalopathies

such as Creutzfeldt–Jakob disease, and are generally referred to as ‘spongiform changes’ [31]. Spongiform encephalopathies are usually infectious diseases caused by prions, and the CNS findings on MRI have been well described in the literature as increased  $T_2$  signal intensity in the affected areas [21,33,34]. Neuronal vacuolization has also recently been described in the pediatric neurosurgery literature where it was observed histologically in the basal nucleus of Meynert in the brains of five infants with hydrocephalus [35]. Another form of human brain vacuolization occurs predominantly in the pyramidal cells of the hippocampus in patients with Alzheimer’s disease [30]. In this ‘granulovacuolar degeneration’, intracytoplasmic vesicles containing a dark center granule and measuring 1–5  $\mu\text{m}$  in diameter were observed within neurons, but the underlying molecular events are poorly understood, and no correlative findings have been described on MRI.

Another explanation offered in the literature for high  $T_2$  values is the gliosis that often accompanies neurodegeneration. In the classic ‘Tiger’s Eye’ finding in the globus pallidus of patients with NBIA Type 1 disease, a hyperintense medial region consistent with gliosis, demyelination, neuronal loss, and axonal swelling is surrounded by a hypointense lateral region where iron accumulation may account for the decreased  $T_2$  signal intensity [14]. In patients with Huntington’s disease, an increased  $T_2$  signal is noted in the putamen, even though this region is known to accumulate significant amounts of iron, and a decrease in signal intensity would therefore be expected. It has been proposed that gliosis or another unknown pathological process is responsible for causing the increased  $T_2$  intensity in Huntington’s patients [7,29]. Similar phenomena may occur in the superior colliculus and substantia nigra of our IRP-2  $-/-$  mice. The significant iron and ferritin demonstrated by our Perls’ DAB and ferritin immunohistochemistry correlate well with the statistically significant increase in low  $T_2$  values, but neuronal degeneration and vacuolization are likely responsible for the notably increased  $T_2$  values.

A key to recognizing that  $T_2$  values in the ROIs of the IRP-2  $-/-$  mice vary across a wider range than in the wild types is the relatively high-resolution achieved in this study. If the resolution had been lower, it is likely that the increased  $T_2$  values associated with vacuolization would have averaged out the low  $T_2$  values associated with ferritin iron accumulation. The fact that the average  $T_2$  values for the ROIs are not significantly different between the IRP-2  $-/-$  and wild-type animals suggests that areas of iron overload in the IRP-2  $-/-$  mice, represented by pixels with low intensity, are intermixed with vacuoles and degenerating neurons, represented by pixels with high intensity. These pixels are all contained within the chosen ROI, making the average  $T_2$  value of the IRP-2  $-/-$  the same as the wild-type ROI, despite the considerable variation in  $T_2$  value distribution between the two groups. Because of the high-resolution we achieved using an 11.7

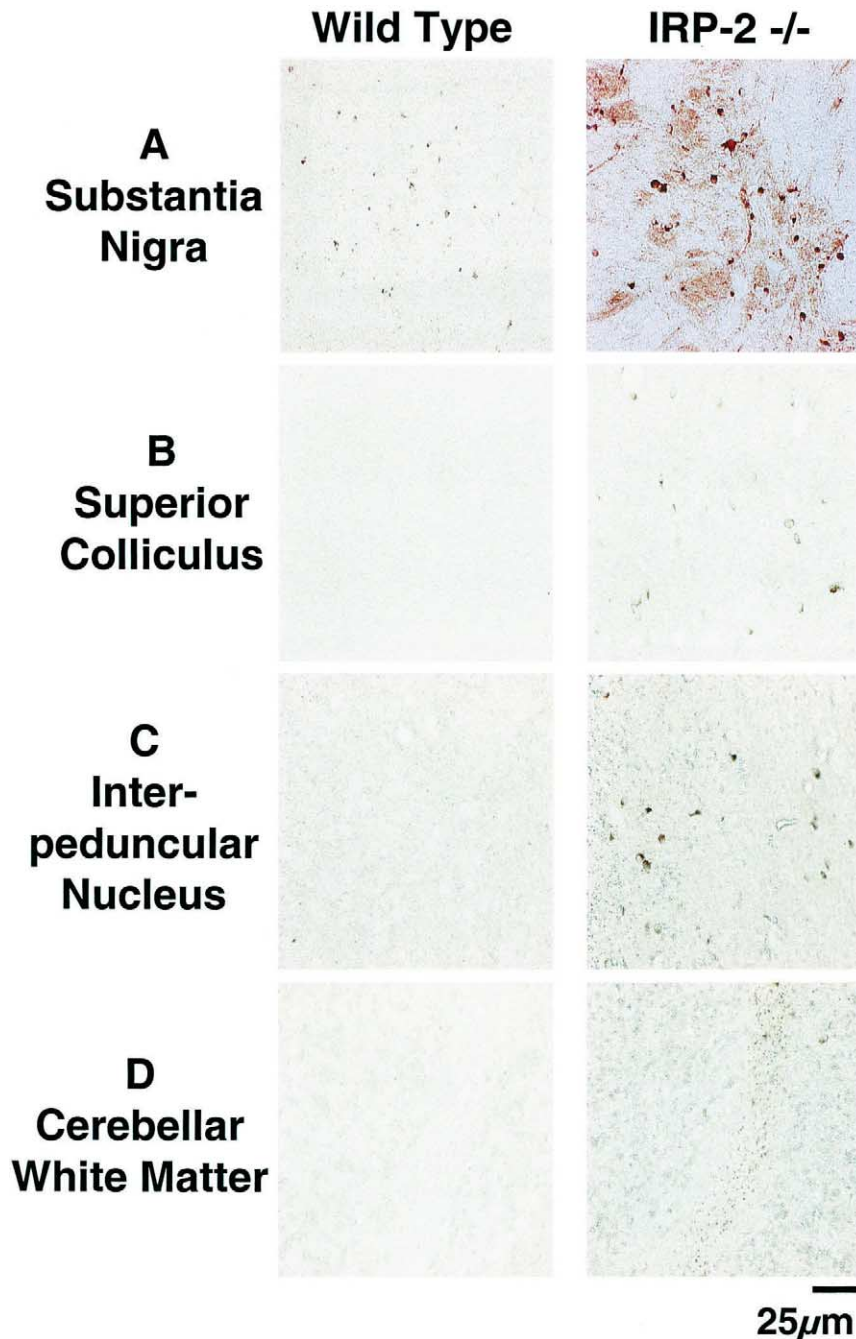


Fig. 4. Detection of ferric iron by histochemistry in regions of interest. Coronal sections of perfused and fixed brains from one of the wild-type mice imaged were stained using the Perls' DAB reaction (left) and compared to the IRP-2  $-/-$  mouse counterpart that was imaged on the same day (right). The four regions of interest shown are the substantia nigra (a), superior colliculus (b), interpeduncular nucleus (c), and cerebellar white matter (d). We were able to consistently identify these four anatomical regions on histological sections by lightly counterstaining the nuclei and using the mouse brain atlas as a reference. Sections of the brain of the IRP-2  $-/-$  mouse show markedly increased ferric iron detected by the Perls' DAB reaction (brown staining) relative to the wild-type mouse.

Tesla magnet and a custom designed receiver coil contoured to fit the mouse skull, the areas of high and low intensity were represented by distinctly different pixels found within the same anatomical region of interest. High-resolution permitted detection of the bimodal histogram pattern of ROIs from IRP-2  $-/-$  mice. A prediction is that the distributions would be even more different be-

tween the IRP-2  $-/-$  and wild-type mice if we further increased the resolution.

A second untested prediction is that if only the older, most severely affected IRP-2  $-/-$  mice were studied, the effect on  $T_2$  distribution might in fact be even more pronounced than the results seen in this study. The phenotypical and histopathological changes begin in IRP-2  $-/-$



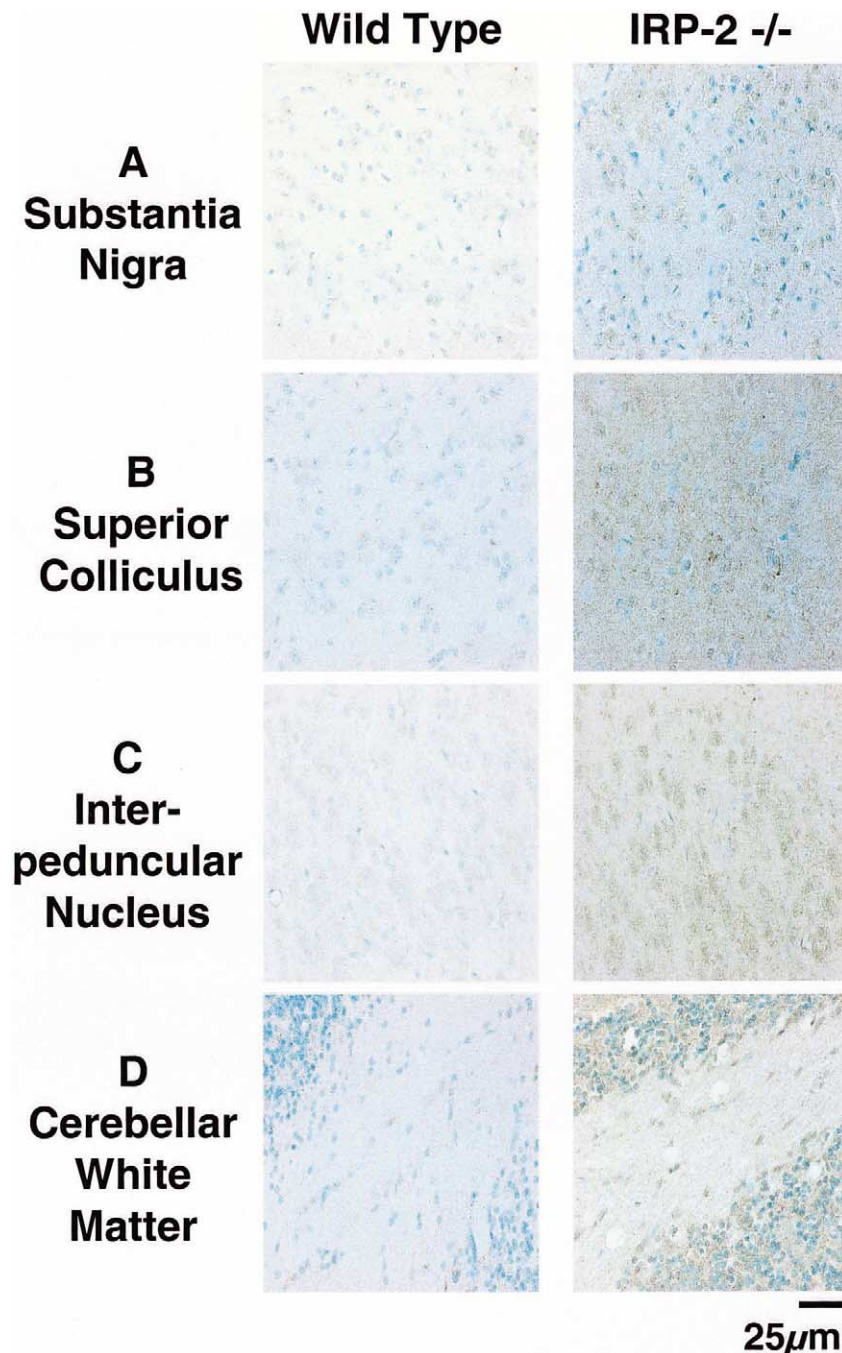


Fig. 5. Ferritin immunohistochemistry of regions of interest. The picture on the left represents ferritin immunohistochemistry performed on coronal sections of the wild-type mouse, and the picture on the right represents ferritin detection in sections from the IRP-2  $-/-$  counterpart imaged on the same day. The four regions of interest shown are the substantia nigra (a), superior colliculus (b), interpeduncular nucleus (c), and cerebellar white matter (d). In each of the regions ferritin expression is compared between the two mice. Immunohistochemical detection of ferritin (brown staining) is clearly increased in the IRP-2  $-/-$  mouse (right) compared to the wild-type (left) in each region of interest.

mice at 6 months and worsen progressively with age, as described in a previous publication [19]. Therefore, 6 months was set as the youngest age of mice eligible for our study. We observed during early pilot MRI studies that due to the progression of neurodegeneration over time and the frailty of the IRP-2  $-/-$  mice, animals older than 14 months did not survive the experimental imaging protocol.

Hence, the upper age limit for this project was set at 14 months. To test the possibility of age-related dilution of our results by including animals from a broad age range, we analyzed the data excluding the three pairs of mice that were less than 9 months of age. We found no significant differences between this data and our original data including all 11 pairs of animals.

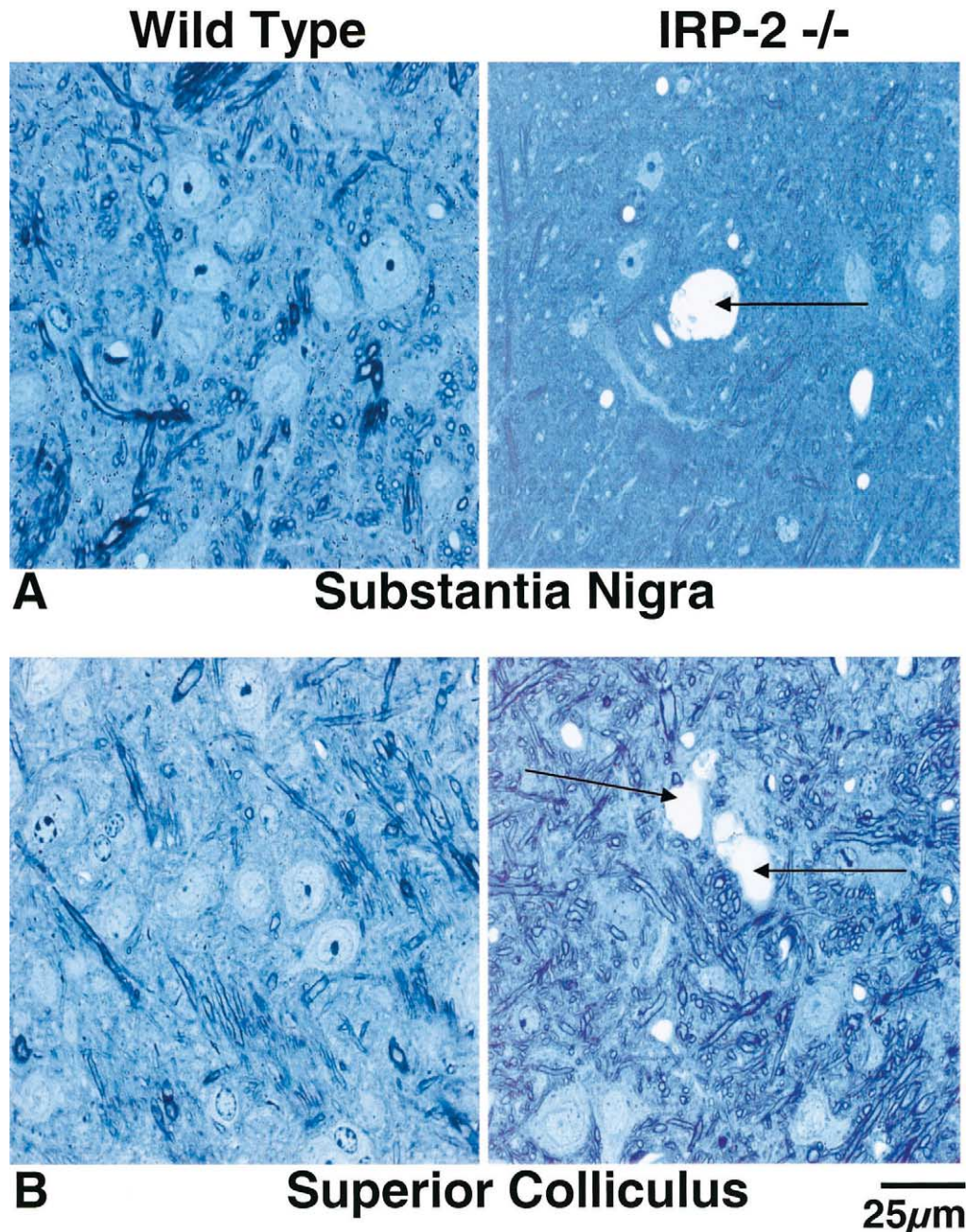


Fig. 6. Vacuolization of the substantia nigra and superior colliculus of IRP-2  $-/-$  mice. Coronal sections of perfused and fixed epoxy embedded brain tissue of a 9-month-old wild type mouse (left) and a 9-month-old IRP-2  $-/-$  mouse (right) were stained with toluidine blue and safranin. Vacuoles were detected throughout the pars compacta region of the substantia nigra (a) as well as in the superior colliculus (b) in the IRP-2  $-/-$  mouse. The arrows indicate vacuoles containing debris and the remnants of a degenerating neuron. A size bar was used to measure the size of the vacuoles, which ranged from 15 to 25  $\mu\text{m}$  in diameter. In many instances the size of the vacuoles was similar to that of neuronal cell bodies.

It may be that with increased resolution on MRI of the human brain, a similar alteration in the pattern of distribution of  $T_2$  values could be found within the brains of patients affected by iron-related neurodegeneration. An association between brain iron deposition and CNS damage has been reported in several neurodegenerative diseases, and iron-dependent oxidative damage may represent a common mechanism of injury. MRI is frequently used to describe patterns of iron accumulation as they relate to

neurodegenerative diseases [18,23,25,36]. However, the limitations of the MRI data gained from these human studies include the lack of matched controls, lower resolution than was achieved in our study, and the difficulty of evaluating histology immediately after completion of the MRI. In the future, the use of stronger magnets may allow increased resolution of human MRI images. Combining higher resolution with histogram analysis such as we used may make it possible to identify changes in the



distribution of  $T_2$  values in affected ROIs of human brains. Careful characterization of  $T_2$  value distribution patterns could aid in the diagnosis of iron-related neurodegenerative diseases, as well as in evaluation of progression and response to treatment.

Our study represents a successful application of magnetic resonance imaging in detection of iron overload and neurodegeneration in a genetically engineered mouse model. By carefully evaluating the data acquired from high-resolution MRI images, we discovered evidence for unexpected pathology in IRP-2  $-/-$  mice that was confirmed histologically. We have described a distinctive MRI pattern that may facilitate the diagnosis and monitoring of human iron-related neurodegenerative diseases. Future studies in our lab will include acquisition of three-dimensional images at higher resolution to trace affected tracts, as well as serial imaging of animals starting in the neonatal period to follow the developmental progression of the disease.

## Acknowledgements

The authors would like to acknowledge the technical assistance of Torri Wilson and Ashley Lakin. This work was supported by the NINDS intramural research program, the intramural program of NICHD, and the Lookout Fund. The views expressed are those of the authors and do not reflect the official policy or position of the USUHS, the Department of Defense or the United States Government.

## References

- [1] P. Aisen, C. Enns, M. Wessling-Resnick, Chemistry and biology of eukaryotic iron metabolism, *Int. J. Biochem. Cell. Biol.* 33 (2002) 940–959.
- [2] G. Anderson, L. Powell, Of metals, mice, and men: what animal models can teach us about body iron loading, *J. Clin. Invest.* 105 (2000) 1185–1186.
- [3] G. Bartzokis, T.A. Tishler, MRI evaluation of basal ganglia ferritin iron and neurotoxicity in Alzheimer's and Huntington's disease, *Cell. Mol. Biol.* 46 (2000) 821–833.
- [4] T. Benner, S. Heiland, G. Erb, M. Forsting, K. Sartor, Accuracy of gamma variate fits to concentration–time curves from dynamic susceptibility-contrast enhanced MRI: influence of time resolution, maximal signal drop and signal-to-noise, *Magn. Reson. Imaging* 15 (1997) 307–317.
- [5] D. Berg, M. Gerlach, M.B.H. Youdin, K.L. Double, L. Zecca, P. Riederer, G. Becker, Brain iron pathways and their relevance to Parkinson's disease, *J. Neurochem.* 79 (2002) 225–236.
- [6] C. Campbell, M. Smith, L. Sayre, S. Bondy, G. Perry, Mechanisms by which metals promote events connected to neurodegenerative diseases, *Brain Res. Bull.* 55 (2001) 125–132.
- [7] J. Chen, P. Hardy, W. Kucharczyk, M. Clauber, J. Joshi, A. Vourlas, M. Dhar, R.M. Henkelman, MR of human postmortem brain tissue: correlative study between  $T_2$  and assays of iron and ferritin in Parkinson and Huntington disease, *Am. J. Neuroradiol.* 14 (1993) 275–281.
- [8] A.R. Curtis, C. Fey, C. Morris, L. Bindoff, P. Ince, P. Chinnery, A. Coulthad, M. Jackson, A. Jackson, D. McHale, D. Hay, W. Barker, A. Markham, D. Bates, A. Curtis, J. Burn, Mutation in the gene encoding ferritin light polypeptide causes dominant adult-onset basal ganglia disease, *Nat. Genet.* 28 (2001) 350–354.
- [9] J. Dehmshki, G.J. Barker, P.S. Tofts, Classification of disease subgroup and correlation with disease severity using magnetic resonance imaging whole-brain histograms: application to magnetization transfer ratios and multiple sclerosis, *IEEE Trans. Med. Imaging* 21 (2002) 320–331.
- [10] D. Dickson, W. Lin, W. Liu, S. Yen, Multiple system atrophy: a sporadic synucleinopathy, *Brain Pathol.* 9 (1999) 721–732.
- [11] B. Drayer, P. Burger, R. Darwin, S. Riederer, R. Herfkens, G.A. Johnson, MRI of brain iron, *Am. J. Roentgenol.* 147 (1986) 103–110.
- [12] M. Gerlach, D. Ben-Shachar, P. Riederer, M.B. H. Youdim, Altered brain metabolism of iron as a cause of neurodegenerative diseases?, *J. Neurochem.* 63 (1994) 793–807.
- [13] M.A. Hayat, in: *Principles and Techniques of Electron Microscopy*, Van Nostrand Reinhold, New York, 1970.
- [14] S. Hayflick, J. Penzien, W. Michl, U. Sharif, N.P. Rosman, P. Wheeler, Cranial MRI changes may precede symptoms in Hallervorden-Spatz syndrome, *Pediatr. Neurol.* 25 (2001) 166–169.
- [15] P. Hilditch-Maguire, F. Trettel, L. Passani, A. Auerbach, F. Persichetti, M. MacDonald, Huntingtin: an iron-regulated protein essential for normal nuclear and perinuclear organelles, *Hum. Mol. Genet.* 9 (2000) 2789–2797.
- [16] J.M. Hill, The distribution of iron in the brain, in: M.B.H. Youdim (Ed.), *Brain Iron: Neurochemical and Behavioral Aspects*, Taylor and Francis, London, 1988, pp. 1–24.
- [17] A.H. Koeppe, The history of iron in the brain, *J. Neurol. Sci.* 134 (Suppl.) (1995) 1–9.
- [18] A. Lang, T. Curran, J. Provias, C. Bergeron, Striatonigral degeneration: iron deposition in putamen correlates with the slit-like void signal of magnetic resonance imaging, *Can. J. Neurol. Sci.* 21 (1994) 311–318.
- [19] T. LaVaute, S. Smith, S. Cooperman, K. Iwai, W. Land, E. Meyron-Holtz, S. Drake, G. Miller, M. Abu-Asab, M. Tsokos, R. Switzer III, A. Grinberg, P. Love, N. Tresser, T. Rouault, Targeted deletion of the gene encoding iron regulatory protein-2 causes misregulation of iron metabolism and neurodegenerative disease in mice, *Nat. Genet.* 27 (2001) 209–214.
- [20] S. Levine, Iron deposits in multiple sclerosis and Alzheimer's disease brains, *Brain Res.* 760 (1997) 298–303.
- [21] Y. Mao-Draayer, S.P. Braff, K.J. Nagle, W. Pendlebury, P.L. Penar, R.E. Shapiro, Emerging patterns of diffusion-weighted MR imaging in Creutzfeldt-Jakob disease: case report and review of the literature, *Am. J. Neuroradiol.* 23 (2002) 550–556.
- [22] C.M. Morris, J.M. Candy, A.E. Oakley, C.A. Bloxham, J.A. Edwardson, Histochemical distribution of non-haem iron in the human brain, *Acta Anat.* 144 (1992) 235–257.
- [23] J.E. Nielsen, L.N. Jensen, K. Krabbe, Hereditary haemochromatosis: a case of iron accumulation in the basal ganglia associated with a parkinsonian syndrome, *J. Neurol. Neurosurg. Psychiatry* 59 (1995) 318–321.
- [24] R.V. Parsey, K.R. Krishnan, A new MRI ratio method for in vivo estimation of signal hypointensity in aging and Alzheimer's disease, *Prog. Neuro-Psychopharmacol. Biol. Psychiat.* 21 (1997) 1257–1267.
- [25] R.V. Parsey, K.R. Krishnan, Quantitative analysis of  $T_2$  signal intensities in Alzheimer's disease, *Psychiatry Res.* 82 (1998) 181–185.
- [26] H. Puccio, D. Simon, M. Cossee, O. Criqui-Filipe, F. Tiziano, J. Melki, C. Hindelang, R. Matyas, P. Rustin, M. Koenig, Mouse models for Friedreich ataxia exhibit cardiomyopathy, sensory nerve defect and Fe-S enzyme deficiency followed by intramitochondrial iron deposits, *Nat. Genet.* 27 (2001) 181–186.
- [27] M. Rausch, K. Scheffler, M. Rudin, E.W. Radu, Analysis of input

- functions from different arterial branches with gamma variate functions and cluster analysis for quantitative blood volume measurements, *Magn. Reson. Imaging* 18 (2000) 1235–1243.
- [28] T. Rouault, R.D. Klausner, Regulation of iron metabolism in eukaryotes, *Curr. Top. Cell. Regul.* 35 (1997) 1–19.
- [29] D.S. Sax, F.S. Buonanno, Putaminal changes in spin-echo magnetic resonance imaging signal in bradykinetic/rigid forms of Huntington's disease, *Neurology* 36 (1986) 311.
- [30] J. Su, J.P. Kesslak, E. Head, C. Cotman, Caspase-cleaved amyloid precursor protein and activated caspase-3 are co-localized in the granules of granulovacuolar degeneration in Alzheimer's disease and Down's syndrome brain, *Acta Neuropathol.* 104 (2002) 1–6.
- [31] M.S. Sy, P. Gambetti, B.S. Wong, Human prion diseases, *Med. Clin. North Am.* 86 (2002) 551–571.
- [32] K. Thompson, S. Shoham, J.R. Connor, Iron and neurodegenerative disorders, *Brain Res. Bull.* 55 (2002) 155–164.
- [33] G.G. Tribl, G. Strasser, J. Zeithofer, S. Asenbaum, C. Jarius, P. Wessely, D. Prayer, Sequential MRI in a case of Creutzfeldt-Jakob disease, *Neuroradiology* 44 (2002) 223–226.
- [34] A. Uemura, T. O'uchi, T. Sakamoto, N. Yashiro, High signal of the striatum in sporadic Creutzfeldt-Jakob disease: sequential change on T2-weighted MRI, *Neuroradiology* 44 (2002) 314–318.
- [35] N. Ulfig, Neuronal vacuolation in the basal nucleus of meynert caused by fetal hydrocephalus, *Pediatr. Neurosurg.* 36 (2002) 320–323.
- [36] J. Vymazal, A. Righini, R. Brooks, M. Canesi, C. Mariani, M. Leonardi, G. Pezzoli, T1 and T2 in the brain of healthy subjects, Patients with Parkinson disease, and patients with Multiple System atrophy: relation to iron content, *Radiology* 211 (1999) 489–495.
- [37] B. Zhou, S. Westaway, B. Levinson, M. Johnson, J. Gitschier, S. Hayflick, A novel pantothenate kinase (PANK2) gene is defective in Hallervorden-Spatz syndrome, *Nat. Genet.* 28 (2001) 345–349.
- [38] H. Zywicke, P. van Gelderen, J. Connor, J. Burdo, M. Garrick, K. Dolan, J. Frank, J. Bulte, Microscopic R2\* mapping of reduced brain iron in the Belgrade rat, *Ann. Neurol.* 52 (2002) 102–105.